

NUWC-NPT Technical Report 12,090
30 March 2012

Energy Absorption Mechanisms in Unidirectional Composites Subjected to Dynamic Loading Events

David B. Segala
Paul V. Cavallaro
Ranges, Engineering, and Analysis Department



**Naval Undersea Warfare Center Division
Newport, Rhode Island**

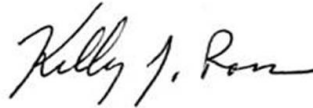
Approved for public release; distribution is unlimited.

PREFACE

This research was funded under NUWC Division Newport's Internal Investment Program, network activity number 300000045014/0010, principal investigator David B. Segala (Code 702). The authors gratefully acknowledge Thomas B. Carroll (Code 70A) for providing the funds for this report.

The technical reviewer was James M. LeBlanc (Code 4121).

Reviewed and Approved: 30 March 2012



Kelly J. Ross
Head, Ranges, Engineering, and Analysis Department



REPORT DOCUMENTATION PAGE

Form Approved
OMB No. 0704-0188

The public reporting burden for this collection of information is estimated to average 1 hour per response, including the time for reviewing instructions, searching existing data sources, gathering and maintaining the data needed, and completing and reviewing the collection of information. Send comments regarding this burden estimate or any other aspect of this collection of information, including suggestions for reducing this burden, to Department of Defense, Washington Headquarters Services, Directorate for Information Operations and Reports (0704-0188), 1215 Jefferson Davis Highway, Suite 1204, Arlington, VA 22202-4302. Respondents should be aware that notwithstanding any other provision of law, no person shall be subject to any penalty for failing to comply with a collection of information if it does not display a currently valid OPM control number.
PLEASE DO NOT RETURN YOUR FORM TO THE ABOVE ADDRESS.

1. REPORT DATE (DD-MM-YYYY) 30-03-2012	2. REPORT TYPE Technical Report	3. DATES COVERED (From – To)
--	---	-------------------------------------

4. TITLE AND SUBTITLE Energy Absorption Mechanisms in Unidirectional Composites Subjected to Dynamic Loading Events	5a. CONTRACT NUMBER
	5b. GRANT NUMBER
	5c. PROGRAM ELEMENT NUMBER

6. AUTHOR(S) David B. Segala Paul V. Cavallaro	5.d PROJECT NUMBER
	5e. TASK NUMBER
	5f. WORK UNIT NUMBER

7. PERFORMING ORGANIZATION NAME(S) AND ADDRESS(ES) Naval Undersea Warfare Center Division 1176 Howell Street Newport, RI 02841-1708	8. PERFORMING ORGANIZATION REPORT NUMBER TR 12,090
---	--

9. SPONSORING/MONITORING AGENCY NAME(S) AND ADDRESS(ES) Naval Undersea Warfare Center Division 1176 Howell Street Newport, RI 02841-1708	10. SPONSORING/MONITOR'S ACRONYM
	11. SPONSORING/MONITORING REPORT NUMBER

12. DISTRIBUTION/AVAILABILITY STATEMENT

Approved for public release; distribution is unlimited.

13. SUPPLEMENTARY NOTES

14. ABSTRACT

This report documents the numerical modeling that was conducted to study the failure modes in dynamically loaded, unidirectional (UD) fibrous composites. The purpose of this research was to determine how to increase energy absorption capacities during severe dynamic loading events. Energy absorption mechanisms are generally composed of elastic, inelastic, kinetic, frictional, acoustic, thermal, and dissipative sources. In this study, the inelastic energy absorption mechanisms associated with damage at the interfacial and constituent levels were numerically characterized through four admissible failure modes: fiber breakage, matrix shearing, fiber/matrix debonding, and fiber/matrix delamination.

Finite element models were developed for cross-ply UD composites constructed of ultrahigh molecular weight polyethylene (UHMWPE) fibers separately reinforced with compliant (Kraton-D polymer) and rigid (epoxy) matrix materials. The energy absorption capacities of these damage mechanisms were contrasted for three different dynamic loading cases including blast, shock, and ballistic impact. The results suggest that the energy loss due to cohesive failure modes is significant for each loading case and, therefore, must be included to ensure model robustness. Fiber breakage and matrix shearing, however—although not significant in blast and shock events—must also be included in ballistic impact cases. Fiber breakage during ballistic impact was the dominant energy absorption mechanism followed by matrix shearing. As is shown for a given perforating ballistic impact case, this study revealed that the epoxy-reinforced laminate captured 4.22% more kinetic energy of the projectile than did the Kraton-reinforced laminate.

15. SUBJECT TERMS
Dynamic Loading Events Energy Absorption Mechanisms Fiber Breakage Fiber/Matrix Debonding Fiber/Matrix Delamination
Matrix Shearing Ultrahigh Molecular Weight Polyethylene Unidirectional Composites

16. SECURITY CLASSIFICATION OF:			17. LIMITATION OF ABSTRACT SAR	18. NUMBER OF PAGES 32	19a. NAME OF RESPONSIBLE PERSON David B. Segala
a. REPORT Unclassified	b. ABSTRACT Unclassified	c. THIS PAGE Unclassified			19b. TELEPHONE NUMBER (Include area code) 401-832-6377

TABLE OF CONTENTS

	Page
LIST OF ILLUSTRATIONS	ii
LIST OF TABLES	iii
LIST OF ABBREVIATIONS AND ACRONYMS	iii
INTRODUCTION	1
Purpose.....	1
Background.....	1
FAILURE MODES.....	3
TWO-PLY QUARTER-SYMMETRY FINITE ELEMENT MODEL	7
Dynamic Loading: Shock	10
Dynamic Loading: Blast	10
Dynamic Loading: Ballistic Impact.....	11
RESULTS	11
DISCUSSION.....	21
CONCLUSIONS.....	23
REFERENCES	24

LIST OF ILLUSTRATIONS

Figure	Page
1 Surface-Based Cohesive Behavior to Model the Interfacial Zone.....	5
2 Hyperelastic Stress Elongation Curve for the Kraton-D Matrix.....	9
3 Left: Surface View of the Two-Ply Model of the Kraton-D Matrix (green) and the UHMWPE Fibers (red); Right: Subset View of the Model Depicting the Mesh Detail Adjacent to Two Fibers.....	9
4 Upper Plot: Overpressure Curve for Dynamic Blast Loading Where the Peak Pressure Was 3000 psi and Decayed Exponentially for 0.5 μ s to 107.0 psi; Lower Plot: Equivalent Force for the Blast Overpressure Event.....	10
5 Von Mises Stress Contours in the Epoxy Matrix (left) and UHMWPE Fibers (right) for the Blast Loading Case (Shown at Time $t = 1.2 \mu$ s)	12
6 Von Mises Stress Contours in the Epoxy Matrix (left) and UHMWPE Fibers (right) for the Shock Loading Case (Shown at Time $t = 1.2 \mu$ s)	12
7 Von Mises Stress Contours in the Epoxy Matrix (left) and UHMWPE Fibers (right) for the Ballistic Loading Case (Shown at Time $t = 1.2 \mu$ s)	13
8 Von Mises Stress Contours in the Kraton-D Matrix (left) and UHMWPE Fibers (right) for the Blast Loading Case (Shown at Time $t = 1.2 \mu$ s)	13
9 Von Mises Stress Contours in the Kraton-D Matrix (left) and UHMWPE Fibers (right) for the Shock Loading Case (Shown at Time $t = 1.2 \mu$ s)	14
10 Von Mises Stress Contours in the Kraton-D Matrix (left) and UHMWPE Fibers (right) for the Ballistic Loading Case (Shown at Time $t = 1.2 \mu$ s)	14
11 Energy Loss Due to Damage for the Epoxy Matrix (A – C) and the Kraton-D Matrix (D – F) for the Blast (top), Shock (middle), and Ballistic Impact (bottom) Loading Events.....	15
12 Depiction of the Cohesive Surfaces for the Top Ply (top row) and Bottom Ply (bottom row) for the Epoxy Material Subjected to Blast (column A), Shock (column B), and Ballistic Impact (column C).....	17
13 Depiction of the Cohesive Surfaces for the Top Ply (top row) and Bottom Ply (bottom row) for the Kraton-D Matrix Material Subjected to Blast (column A), Shock (column B), and Ballistic Impact (column C).....	18
14 Projectile Velocity of the Kraton-D (blue line) and Epoxy (red line) Matrix	19
15 Percentage of the Projectile Kinetic Energy Absorbed by the Epoxy (red line) and Kraton-D (blue line) Composite Laminate	20
16 Top Row: Percentage of the Energy Absorption Mechanisms of the Composite Laminate Including Damage Dissipation (blue line), Frictional Dissipation (green line), Kinetic Energy of the Composite (red line), Plastic Dissipation (cyan line), Strain Energy (magenta line), and Viscous Dissipation (yellow line) for the Epoxy (column A) and Kraton-D (column B) Matrix Materials Subjected to Ballistic Loading; Bottom Row: Energy Balance (cyan line) Showing the Sum of the Energy Absorbed by the Composite (blue line) and the Kinetic Energy of Projectile (red line).....	20

LIST OF TABLES

Table	Page
1 Stiffness and Displacement Properties for the Cohesive Surfaces	6
2 Hyperelastic Kraton-D Matrix Material Properties	7
3 Isotropic Material Properties for UHMWPE Fibers	7
4 Epoxy Resin Matrix Material Properties	7
5 Material Properties for the Steel FSP.....	11

LIST OF ABBREVIATIONS AND ACRONYMS

3-D	Three-dimensional
FE	Finite element
FSP	Fragment simulating projectile
IED	Improvised explosive device
MMOD	Micrometeor orbital debris
NASA	National Aeronautics and Space Administration
SIS	Styrene-isoprene-styrene
UD	Unidirectional
UHMWPE	Ultrahigh molecular weight polyurethane

ENERGY ABSORPTION MECHANISMS IN UNIDIRECTIONAL COMPOSITES SUBJECTED TO DYNAMIC LOADING EVENTS

INTRODUCTION

PURPOSE

This report documents the numerical modeling that was conducted to study the failure modes in dynamically loaded, unidirectional (UD) fibrous composites. The purpose of this research was to investigate the energy absorption capabilities of admissible failure modes for a cross-ply UD composite laminate subjected to severe dynamic loading events including blast, shock, and ballistic impact.

Four failure mechanisms were considered, namely fiber breakage, matrix shearing, fiber/matrix debonding, and fiber/matrix delamination (that is, cohesive interfacial failure). Two matrix materials were evaluated, namely a rigid epoxy and a compliant elastomer (Kraton-D). The reinforcing fiber material was ultrahigh molecular weight polyethylene (UHMWPE).

BACKGROUND

Fiber-reinforced composites have become an integral part of commercial, recreation, and defense markets. The proliferation of applications for fiber-reinforced composite technology can be in large part attributed to tailorability—the single-most advantageous aspect of fiber-reinforced composites. Specifically, tailorability provides the designer with unique levels of customization, such as selection of the fiber and matrix materials, lamina architecture, and laminate stacking schedules and orientations—all of which facilitate the design of a composite with optimal product performance with minimal weight.

The diverse requirements for various military/defense composite applications demonstrate (1) how challenging it is to design a functional composite that offers optimum protection for vehicles, vessels, buildings, and even personnel and (2) how critical tailorability is to that design process. For example, military land vehicles are often suited with hard armor composites to withstand ballistic impacts from enemy combatants and blasts from improvised explosive devices (IEDs); marine vessels, however, require protection from blast overpressures, shock, wave slap, electromagnetic threats, and corrosion. Blast-resistance composites and fabrics are being deployed in building construction, temporary shelters, and spall liners as barriers for defeating fragment threats. The National Aeronautics and Space Administration (NASA) uses ballistic composite laminates and fabrics for its deep-space habitats to protect against micrometeor orbital debris (MMOD), which travel at hyper velocities (> 3 km/sec). Personnel armor, both soft and hard, range from stab-resistant vests, to vests designed to withstand .50 caliber armor-piercing ammunition, to blast-resistance diapers for vehicle

personnel and for demolition and mine-clearing troops. Cavallaro^{1,2,3} provides an overview of personnel armors and research that has been conducted on plain-woven soft body armors.

The growth of composites in high-performance markets continues to outpace the development of new and improved physics-based modeling methods. Rather, current design tools for severe, dynamically loaded composite structures, which continue to lag at the constituent and interfacial levels, lack the robustness required to suitably predict performance prior to manufacturing and prototype testing. Because this deficiency confines the development cycle to the costly and time-excessive *build-test-build* approach, it is imperative that research to develop robust numerical finite element (FE) tools capable of capturing stress wave propagations and energy absorption mechanisms in dynamically loaded UD composites be pursued.

The tailorability features afforded by composites include hosts of different fiber materials (for example, aramids, polyethylenes, polyesters, glasses, and ceramics) and matrix materials (for example, polymers, ceramics, and metals) from which the designer can choose. Also available are ranges of mechanical properties for the fiber and matrix materials, such as density, strength, elongation, modulus, toughness, strain rate dependencies—all of which have the propensity to influence the stress wave propagations and energy absorption capacities at the meso-scale. Crimp imbalance, which represents one architectural modification that can be specified/tailored in woven composites and fabrics, can be used to selectively alter stress wave dynamics.² Similarly, lamina stacking schedules (for example, 0/90, 0/45/90/−45, 0/45/0, etc.) and thicknesses^{4,5,6} can be changed to alter (1) how the stress waves propagate along the in-plane and through-thickness directions of the laminate and (2) the extent that reflections occur at the lamina boundaries at the macro-scale.

Batra and Hassan developed custom FE software⁷ to subject UD composites to dynamic loading events such as blast⁸ and shock⁹ for various geometric, loading, and material properties. For UD composites subjected to blast, it was shown that approximately 15% of the work done by external forces was dissipated through four failure modes and the stacking sequence strongly influenced the energy dissipation. The same conclusions were drawn for shock loading, with the addition that fiber orientation influenced both the time and location of failure mode initiation and its direction of propagation. In both models, delamination served as the damage mechanism that absorbed the most energy; however, Batra and Hassan pointed out that (1) the software homogenized the damage energies so that the energies associated with each failure mode were easily obtained and (2) only three internal damage variables were used but four failure modes were computed. The internal damage variables were used to simulate matrix cracking, fiber breakage, and fiber/matrix debonding. A failure envelope was used to model the initiation of delamination of the adjoining layers. The failure modes not considered were fiber pull-out, fiber kinking, fiber buckling, and matrix crushing.

Dolce et al.¹⁰ developed a three-dimensional (3-D) FE model of a carbon fiber-reinforced plastic composite plate subjected to blast loads from C4 explosive charges along with experimental testing. The model, which agreed reasonably well with experimental data, considered only delamination based on the Dycoss Discrete Crack Model between the layers in the composite and the Chang-Chang failure criteria for modeling in-plane failure of the UD

layers. All four failure modes, however, were not taken into account in the model, which may be one explanation for the difference in matching numerical results with experimental results.

Will et al.¹¹ investigated the effects of laminate stacking of carbon fiber-reinforced polymers subjected to projectile impact. Their research revealed that, in high-speed impacts, a structure deformed locally and little energy was used to deform fibers and the structure. Furthermore, a significant amount of energy was dissipated in delamination, debonding, and fiber pull-out.

Other researchers^{7, 12, 13, 14} developed cohesive elements to model damage initiation and damage evolution in the fiber/matrix interfacial zone. Karahan¹⁵ compared the ballistic performance and energy absorption in woven and UD aramid fabrics. Although this study showed that the UD fabric panels absorbed 12.5% – 16.5% more energy of the projectile than did the woven fabric for unit panel weights, the fibers used were not the same.

In the automotive industry, Jacob et al.¹⁶ reviewed the energy absorption of polymer composites for human safety in automotive crash events. It was found that the energy absorption by the fiber was dependent on the fiber density. In addition, the energy absorption capacity increased with increasing interlaminar fracture toughness. As for the fiber-volume ratio, as the interlaminar strength decreased, interlaminar cracks formed at lower loads, which resulted in a reduced energy absorption capability. The density of the composite increases with increasing fiber-volume fraction, which results in a lower energy absorption capability of the composite.

Extensive research has been conducted to address energy absorption behaviors in rigid UD composites subjected to various dynamic loads; however, limited knowledge exists regarding the capacities of energy absorption mechanisms in composites constructed with compliant matrix materials. Moreover, the current literature lacks sufficient descriptions of the dominant failure mechanisms, failure energy thresholds, and limits for severe transient loadings.

The purpose of this research was to demonstrate that the dominant failure mechanisms that absorb the most energy are dependent on the type of dynamic loads and, therefore, the designer must fully know, *a priori*, the loading definitions for developing a robust FE model for predicting the dynamic response of the composite structure.

FAILURE MODES

The prevailing consensus of the scientific community considers fiber breakage, matrix shearing/cracking, and fiber/matrix debonding and delamination to be the primary failure mechanisms of composites. With proper selection of the constituent materials and their respective strengths, stiffnesses, and interfacial (cohesive) strengths, the designer can tailor the thresholds, limits, and sequencing of failure modes to enhance the dynamic energy absorptions and stress wave propagations in the composite structure.

Fiber-reinforced composites are often designed so that the fibers bear the in-plane normal forces if the composite is impacted in the longitudinal direction. In this scenario, therefore, the fibers may be first to fail. In the event that the fibers are loaded with some prescribed force, a shear stress will develop down the length of the fiber in the interfacial (cohesive) zone. If the shear stress induced from the impact is greater than the shear strength of the cohesive bond, the bond will fail and will release strain energy—leading to a higher concentration of shear stress at the particular point. This fiber/matrix debonding is more prominent if the bond is relatively weak. If, however, the bond is relatively strong, the matrix will fail due to shear and the failure will extend along the matrix parallel to the fiber. As the fiber continues to break in different locations, the fiber will eventually delaminate from the matrix in its entirety. Once the fiber starts to delaminate from the matrix, the classic fiber pull-out problem becomes an issue, as described by shear lag theory.^{4,6} Once the fiber is completely delaminated from the matrix, the matrix transfers the load to the surrounding fibers. There are many theories describing the process of load transfer to neighboring fibers, a review of which can be found in Brondsted's⁴ article.

Modeling the interfacial zone requires an understanding of cohesive failure mechanics (that is, fiber/matrix debonding and delamination) and traction versus separation cohesive elements/surfaces. Cohesive surfaces were used because it was assumed that the cohesive layer resembles a thin film with zero thickness. To implement cohesive surfaces into the FE model, a surface was created around the outside of the fiber and a surface was created around the inside of the matrix where the fiber is nested. Initially, these two surfaces are bonded together and have a cohesive stiffness in the normal (K_n) and two shear directions (K_s and K_t). By using a damage initiation and evolution law, degradation and eventual failure of the bond between both cohesive surfaces can be simulated. Once the bond fails at a particular interfacial point, the two surfaces at that point are no longer bonded together and cannot adhere to any other point on either cohesive surface. In other words, once an interfacial point fails (that is, the bond breaks), the adhesive characteristics at that point are lost and irreversible.

The contact stress or traction t is defined as the contact force divided by the current area at each contact (interface) point. The separation is merely just the separation distance between the contact surfaces.

A linear elastic traction-separation damage model is used to model the cohesive failure modes for the cohesive surfaces as shown in figure 1. The slope of the first part of the curve is $K_n(K_s, K_t)$, which represents the normal and tangential cohesive surface stiffness components, respectively. Refer to table 1 for the stiffness values.

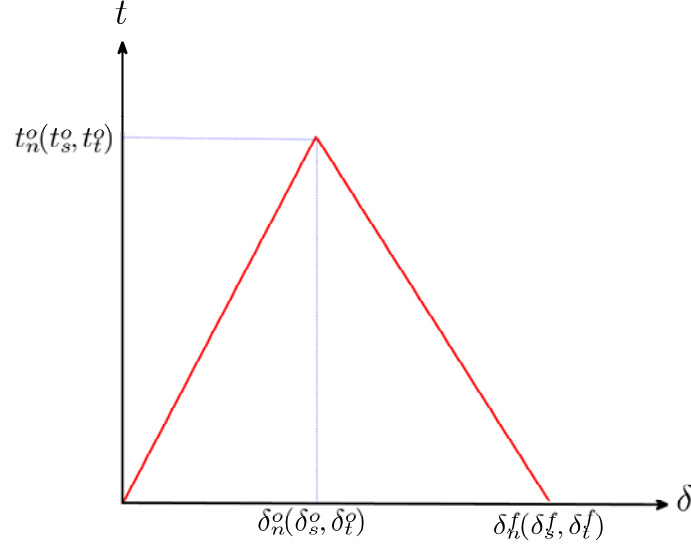


Figure 1. Surface-Based Cohesive Behavior to Model the Interfacial Zone
 (The contact stresses at damage initiation are $t_n^o(t_s^o, t_t^o)$ and effective separation at damage initiation $\delta_n^o(\delta_s^o, \delta_t^o)$. The separations at failure are $\delta_n^f(\delta_s^f, \delta_t^f)$ where subscripts n , s , and t refer to the normal and tangential directions, respectively.)

The linear damage initiation, up to δ^o in figure 1, is based on a maximum separation criterion, which is expressed in equation (1) as

$$\max \left\{ \frac{\langle \delta_n \rangle}{\delta_n^o}, \frac{\delta_s}{\delta_s^o}, \frac{\delta_t}{\delta_t^o} \right\} = 1, \quad (1)$$

where δ_n is the separation in the pure normal direction,

δ_s is the separation in the first shear direction,

δ_t is the separation in the second shear direction,

δ_n^o , δ_s^o , and δ_t^o are the effective separations at damage initiation, and

$\langle \cdot \rangle$ represents Macaulay brackets.

Once the separation criterion is met in equation (1) (refer to table 1), the contact point between both cohesive surfaces has separated so that the process of degradation begins by the assigned damage evolution law.

A linear damage evolution law based on displacements is used in this study and is represented by the second half of the curve in figure 1. As mentioned, the damage evolution for cohesive surfaces describes the degradation of the cohesive stiffness. A scalar damage variable D represents the overall damage at the contact point with an initial value of zero. The contact stress components are a function of the damage variable and are defined in equations (2) through (4):

$$\begin{aligned}
t_n &= \begin{cases} (1-D)\bar{t}_n, & \bar{t}_n \geq 0 \\ \bar{t}_n, & \text{otherwise (no damage to compressive stiffness)} \end{cases} \\
t_s &= (1-D)\bar{t}_s, \\
t_t &= (1-D)\bar{t}_t,
\end{aligned} \tag{2}$$

where \bar{t}_n , \bar{t}_s , and \bar{t}_t are the contact stress components without damage. The value of D is

$$D = \frac{\delta_m^f (\delta_m^{\max} - \delta_m^o)}{\delta_m^{\max} (\delta_m^f - \delta_m^o)}, \tag{3}$$

and where

$$\delta_m = \sqrt{\langle \delta_n \rangle^2 + \delta_s^2 + \delta_t^2}, \tag{4}$$

is the maximum value of the effective separation attained during the loading history, and $\delta_m^f - \delta_m^o$ is specified as the difference between the separation at failure and initiation at a contact point.

Table 1. Stiffness and Displacement Properties for the Cohesive Surfaces

K_n Kn(psi)	K_s Ks(psi)	K_t (psi)	δ_n^o (in.)	δ_n^o (in.)	δ_n^o (in.)	δ_n^f (in.)	δ_n^f (in.)	δ_n^f (in.)
8.0E5	8.0E5	8.0E5	1.7E-5	1.7E-5	1.7E-5	3.0E-5	3.0E-5	3.0E-5

The same approach as was described for the cohesive surfaces was taken to model both fiber breakage and matrix shearing—except for how damage initiation is defined. Damage initiation is based on a shear failure strain or an equivalent plastic strain. The equivalent plastic strain, a scalar value, is defined in ABAQUS as shown in equation (5):

$$\bar{\varepsilon}^p = \int_0^t \dot{\varepsilon}^p dt, \tag{5}$$

where $\dot{\varepsilon}^p$ is the plastic strain rate and defined in equation (6) as

$$\dot{\varepsilon} = \sqrt{\frac{2}{3} \dot{\varepsilon}_{ij}^p \dot{\varepsilon}_{ij}^p}. \tag{6}$$

The plastic strain rate is deviatoric with

$$\dot{\epsilon}_{11}^p = \dot{\epsilon}_{22}^p = -\frac{\dot{\epsilon}}{2}, \dot{\epsilon}_{33}^p = -\frac{\dot{\epsilon}}{2} \text{ therefore } \sum_{i=1}^3 \dot{\epsilon}_{ii}^p = 0, \quad (7)$$

and all shear strain rates are zero. Once the equivalent plastic strain value is reached for damage initiation, the same displacement-based evolution law, as described previously for the cohesive damage evolution, is used.

TWO-PLY QUARTER-SYMMETRY FINITE ELEMENT MODEL

A FE model of a quarter-symmetric (0/90) UD fibrous composite laminate was developed and simulated using ABAQUS/Explicit.¹⁷ Two separate models, each with different matrix materials, were used. The first model was a soft, compliant polymer (Kraton-D), and the second was a hard epoxy resin (refer to tables 2 and 3 for material properties). Each model was reinforced with UHMWPE fibers whose material properties are listed in table 4.

Table 2. Hyperelastic Kraton-D Matrix Material Properties

E E(psi)	ρ (lb/in. ³)	Ultimate Strength (psi)	$\bar{\epsilon}^p$ (in./in.)	δ^f (in.)
See figure 2	8.59E-5	2800	1.5	2.0E-5

Table 3. Isotropic Material Properties for UHMWPE Fibers¹⁸

E (psi)	ν	ρ (lb/in. ³)	Ultimate Strength (psi)	$\bar{\epsilon}^p$ (in./in.)	δ^f (in.)
17,110,000.0	.3	1.3E-4	580,000	0.36	1.0E-5

Table 4. Epoxy Resin Matrix Material Properties

E (psi)	ν	ρ (lb/in.)	Ultimate Strength (psi)	$\bar{\epsilon}^p$ (in./in.)	δ^f (in)
435,113.0	.4	1.68E-4	13,900	2.5	2.0E-5

The Kraton-D polymer is a styrene-isoprene-styrene (SIS) hyperelastic elastomer. The stress elongation curve is depicted in figure 2; its ultimate strength of 2800 psi at 1200% elongation was included in the material model for matrix failure. The hyperelastic strain energy potential was obtained using ABAQUS by a third-order Marlow model. The epoxy resin was modeled as an isotropic material with an ultimate strength of 13,900 psi. The UHMWPE fibers, 25 per ply, were given a diameter of 0.0011 inch (28 μm) and a length of 0.025 inch (635 μm); they were modeled as an isotropic material. The authors acknowledge that these fibers exhibit orthotropic behavior; however, the failure mechanisms in ABAQUS were limited to isotropic material behavior.

All elements for both the fiber and matrix were modeled with eight-node linear brick continuum elements with incompatible modes (ABAQUS type C3D8I). The characteristic length of an element is 0.0001 inch.

The models shown in the present analyses were constructed using quarter-symmetric representations that were permissible provided that the material properties, displacement boundary conditions, and applied loads were collectively quarter-symmetric. In figure 3, the quarter-symmetry planes are the YZ- and YX-planes. The boundary conditions were such that no translations normal to the planes were admissible. The key advantage to using quarter-symmetric representations is reduced computational time with no loss of solution robustness. Because of the relatively small dimensions of the fiber cross sections, ply thicknesses, and the level of mesh discretization applied, the solution time increment was on the order of 4E-11 second.

The ABAQUS/Explicit solver computes a solution time increment based on the dilatational wave speed in the materials used and the smallest characteristic element length according to

$$\Delta t \approx \frac{L_{\min}}{c_d},$$

where L_{\min} is the characteristic length of the smallest element and c_d is the dilatational wave speed defined as

$$c_d = \sqrt{\frac{E}{\rho}},$$

where ρ is the material density and E is Young's modulus.

General contact surfaces and surface interactions (hard overpressure) were established between the matrix and fibers and between the fibers with each other. For the ballistic impact case, contact was defined for the matrix and fragment simulating projectile (FSP) as well as the fibers and FSP. It was necessary to establish contact between the fibers and FSP because, as the matrix material degraded due to failure, the FSP came into contact with the fibers. If fiber-to-FSP contact was not established, the FSP would simply pass through the fibers.

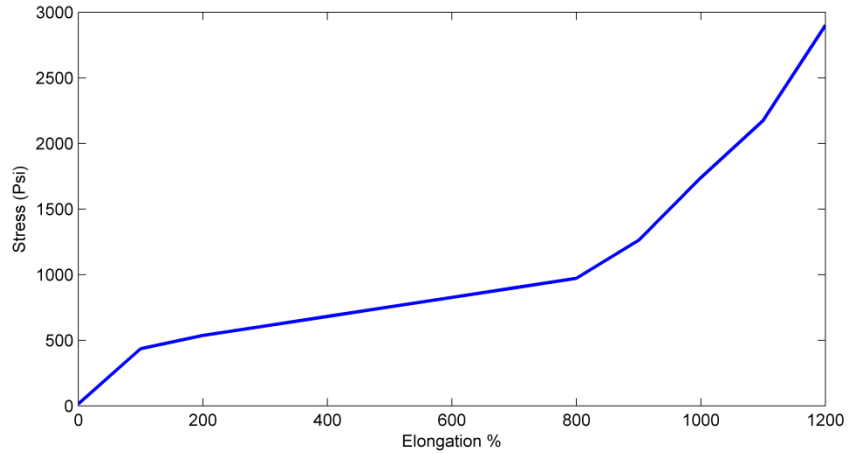


Figure 2. Hyperelastic Stress Elongation Curve for the Kraton-D Matrix

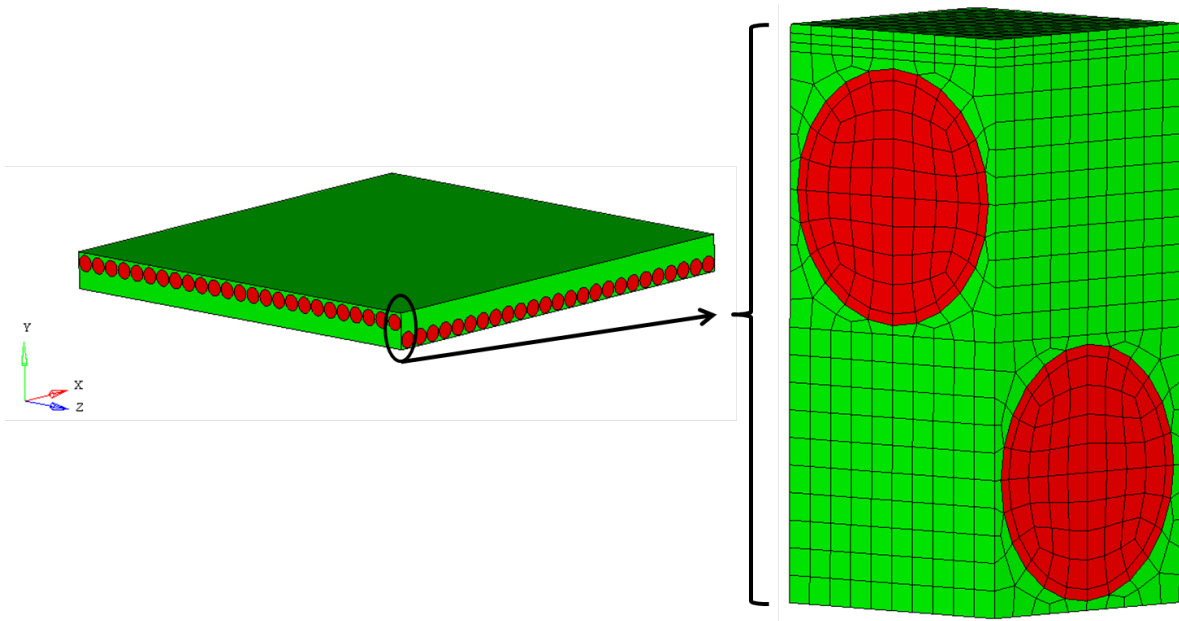


Figure 3. Left: Surface View of the Two-Ply Model of the Kraton-D Matrix (green) and the UHMWPE Fibers (red); Right: Subset View of the Model Depicting the Mesh Detail Adjacent to Two Fibers

DYNAMIC LOADING: SHOCK

The shock event was described by applying an initial velocity to the model at the nodes along the YZ-plane in the negative X-direction. The magnitude of the initial velocity was 24,000 in./s (2000 ft/s).

DYNAMIC LOADING: BLAST

The blast event was described by applying an overpressure to the upper lamina along the XZ-plane in the negative Y-direction. The overpressure time-history is depicted in the upper plot of figure 4 and defined by equation (8). The equivalent force-time history (based on XZ-surface area) is shown in the lower plot of figure 4. The maximum peak pressure was 3000 psi, which decayed exponentially for 0.5 μ s where it reaches a sustained value of 107.0 psi for the remaining duration of the solution.

$$P(t) = 3000 \exp(-t/1.5). \quad (8)$$

Because the model was relatively small, achieving any deformation required a significant pressure to be used considering that the surface area was 0.000625 in.²—resulting in an applied force of only 1.875 lb.

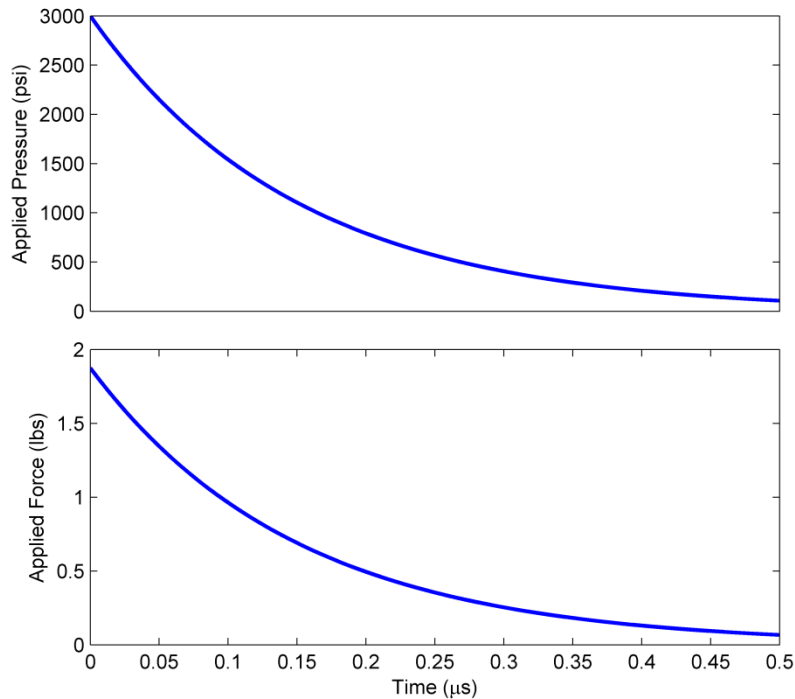


Figure 4. Upper Plot: Overpressure Curve for Dynamic Blast Loading Where the Peak Pressure Was 3000 psi and Decayed Exponentially for 0.5 μ s to 107.0 psi; Lower Plot: Equivalent Force for the Blast Overpressure Event

DYNAMIC LOADING: BALLISTIC IMPACT

To simulate a ballistic impact event, a quarter-symmetric representation of a non-deformable FSP was used. The FSP was composed of steel and was modeled as a rigid body using six-node linear triangular prism continuum elements (ABAQUS type C3D6). The material properties for steel are listed in table 5. A reference node on the FSP was driven by an initial velocity of 12,000 in./s (1000 ft/s). The assumed static coefficients of friction used between the fibers, matrix, and FSP was $\mu_s = 0.1$.

Table 5. Material Properties for the Steel FSP

E (psi)	ρ (lb/in. ³)	ν	Mass (lb)
3.0E7	7.686E-4	1.0E-3	1.313E-10

RESULTS

The FE models described in this report are representative of soft and hard UD composite laminates. The matrix materials consisted of a hard epoxy and soft Kraton-D, and the fibers were restricted to UHMWPE fibers. Both laminate models were subjected to identical blast, shock, and ballistic loading events to investigate their energy absorption capabilities and damage mechanisms. Four failure mechanisms including fiber breakage, matrix shearing, and fiber/matrix interfacial debonding and delamination were considered. Each model was simulated for 1.2 μ s.

Figures 5 through 7 depict the Von Mises stress contours for the blast, shock, and ballistic loading cases for the epoxy (hard) matrix, respectively; figures 8 through 10 depict the Von Mises stress contours for the blast, shock, and ballistic loading cases for the Kraton-D (soft) matrix, respectively. For these six illustrations, the plots on the right show only the fiber elements, and the plots on the left show only the matrix elements.

The Von Mises stress contours for the epoxy matrix models blast and ballistic impact cases (see figures 5 and 7), achieved maximum values nearly equal to the specified ultimate strengths for both the matrix and fiber materials. For the fibers, the ultimate strength was reached in the ballistic case (figure 7) and is nearly developed in the blast case (figure 6). The peak stress level in the shock case did not achieve the ultimate strength of the matrix and fiber.

The Von Mises stress in the Kraton-D matrix did not reach the ultimate strength in the loading cases that were considered because of the material's hyperelasticity; specifically, the hyperelasticity of the Kraton-D matrix required that the material strain to 1200% to achieve its ultimate stress. The ultimate stress of the fibers was reached in both the blast (figure 8) and ballistic (figure 10) impact cases. The maximum Von Mises stress of the fibers during the shock event (figure 9) nearly achieved the ultimate stress.

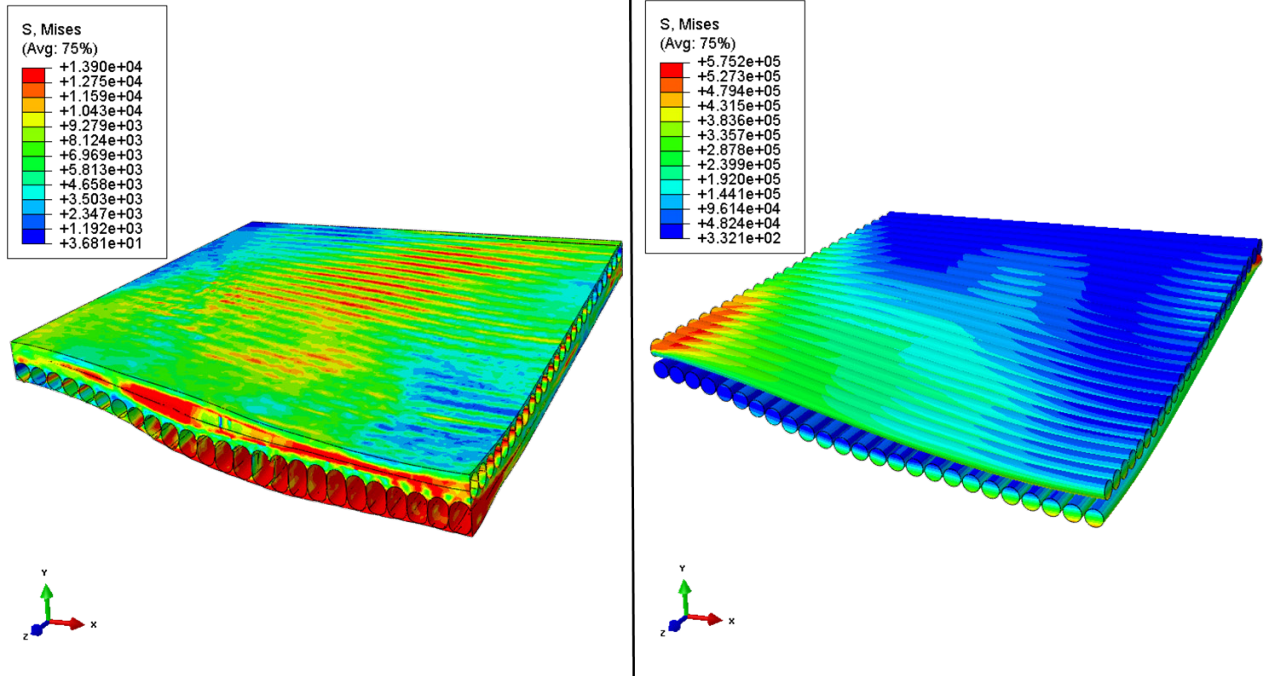


Figure 5. Von Mises Stress Contours in the Epoxy Matrix (left) and UHMWPE Fibers (right) for the Blast Loading Case (Shown at Time $t = 1.2 \mu s$)

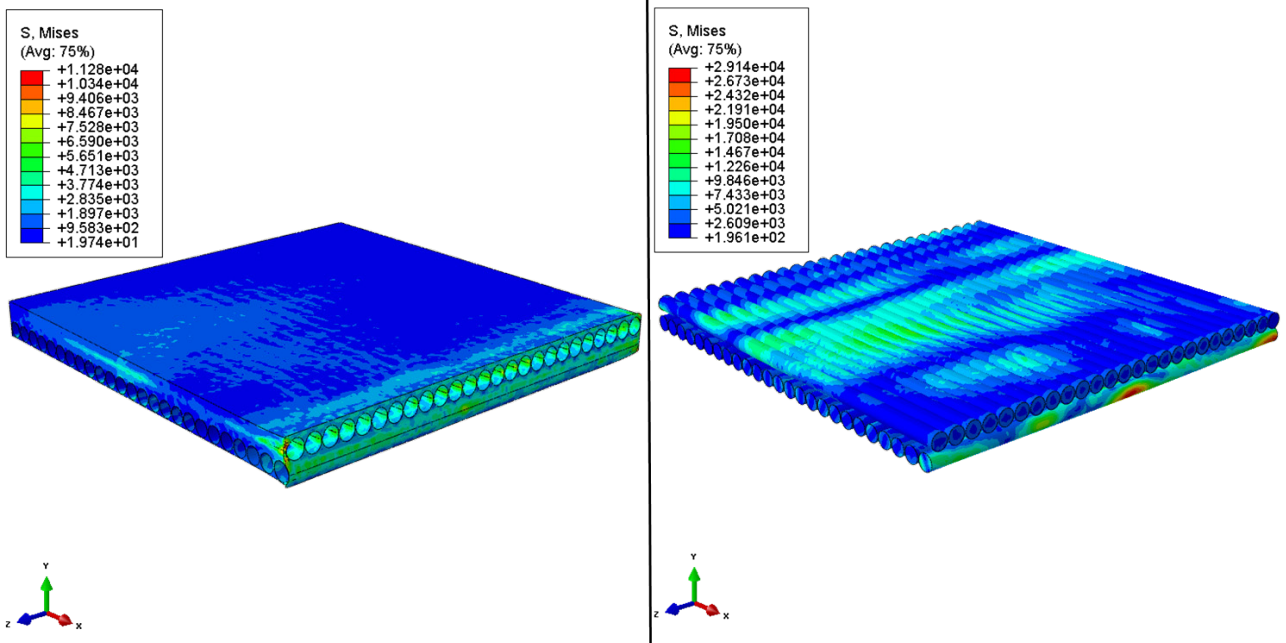


Figure 6. Von Mises Stress Contours in the Epoxy Matrix (left) and UHMWPE Fibers (right) for the Shock Loading Case (Shown at Time $t = 1.2 \mu s$)

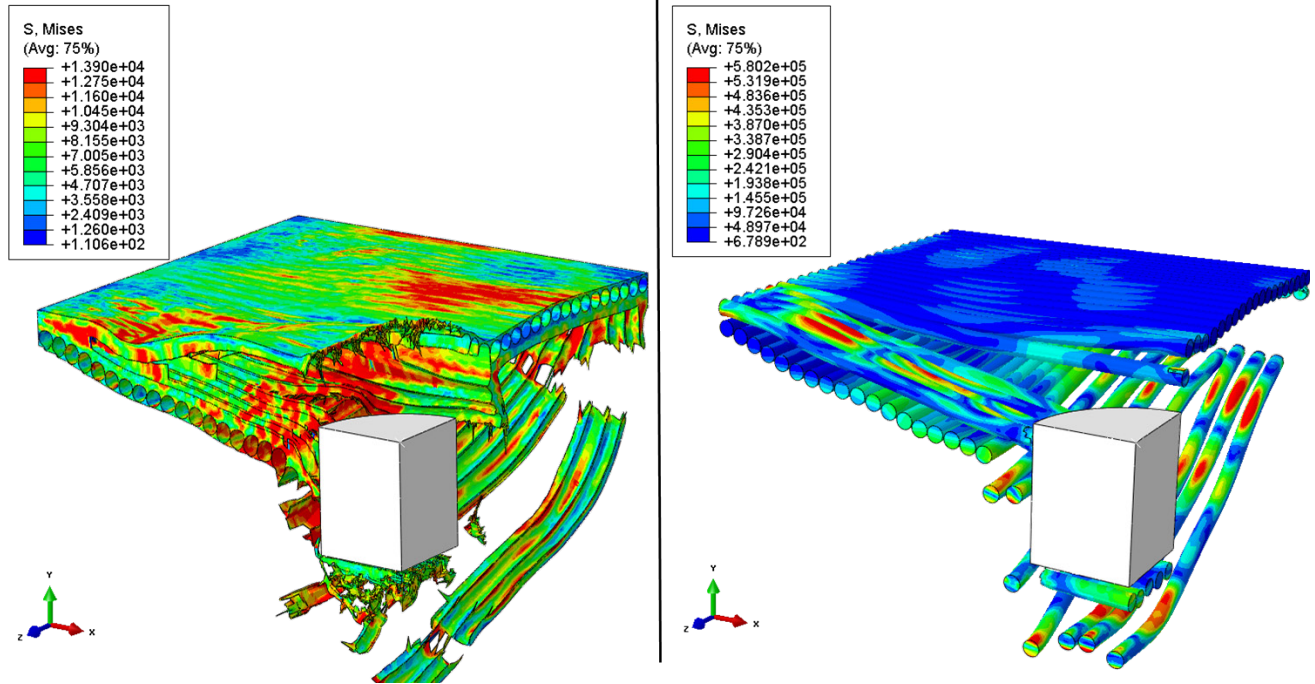


Figure 7. Von Mises Stress Contours in the Epoxy Matrix (left) and UHMWPE Fibers (right) for the Ballistic Loading Case (Shown at Time $t = 1.2 \mu s$)

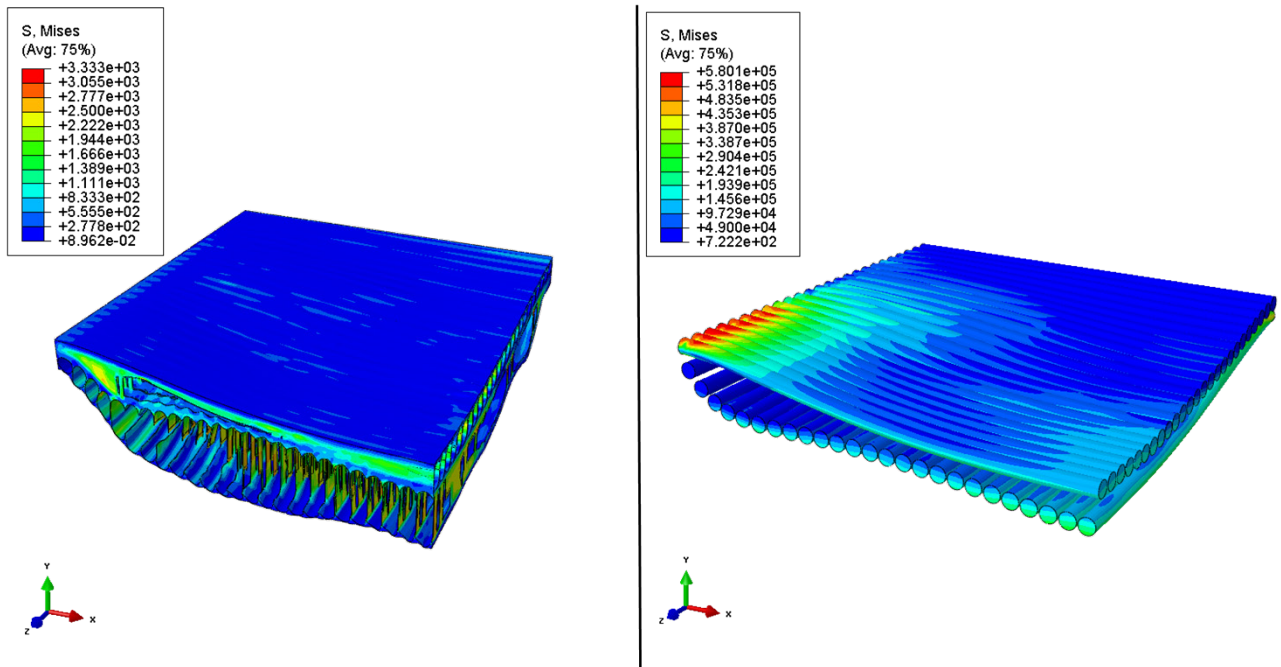


Figure 8. Von Mises Stress Contours in the Kraton-D Matrix (left) and UHMWPE Fibers (right) for the Blast Loading Case (Shown at Time $t = 1.2 \mu s$)

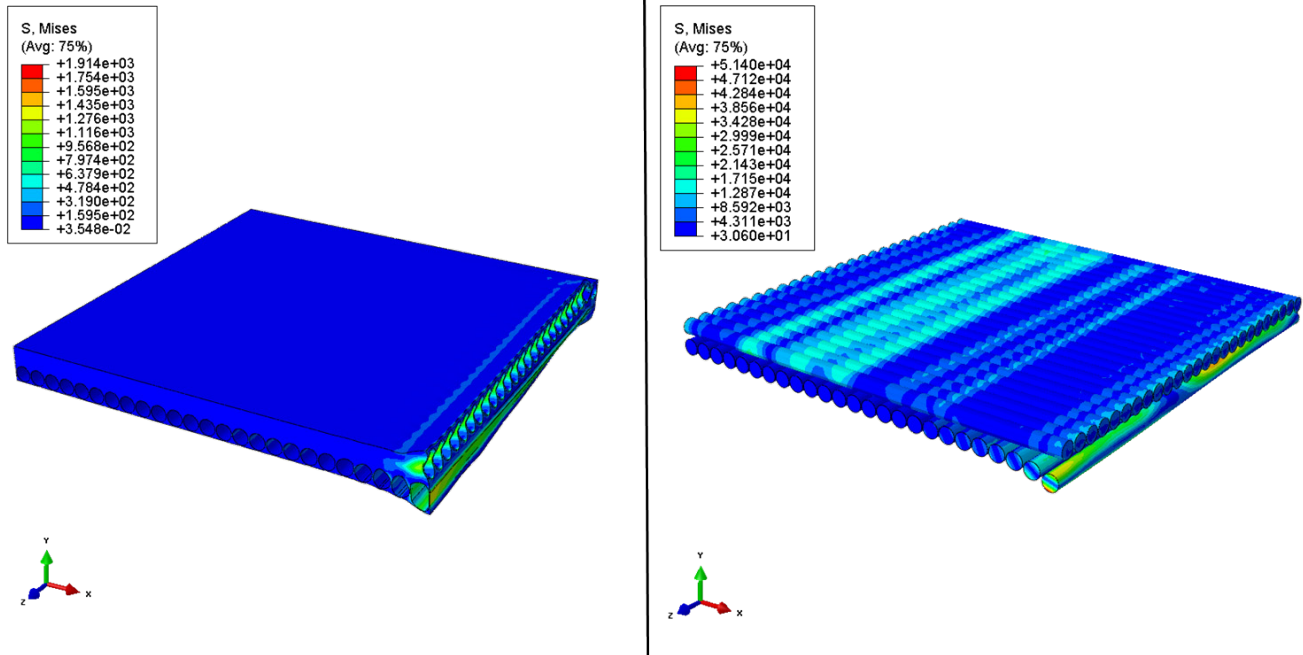


Figure 9. Von Mises Stress Contours in the Kraton-D Matrix (left) and UHMWPE Fibers (right) for the Shock Loading Case (Shown at Time $t = 1.2 \mu s$)

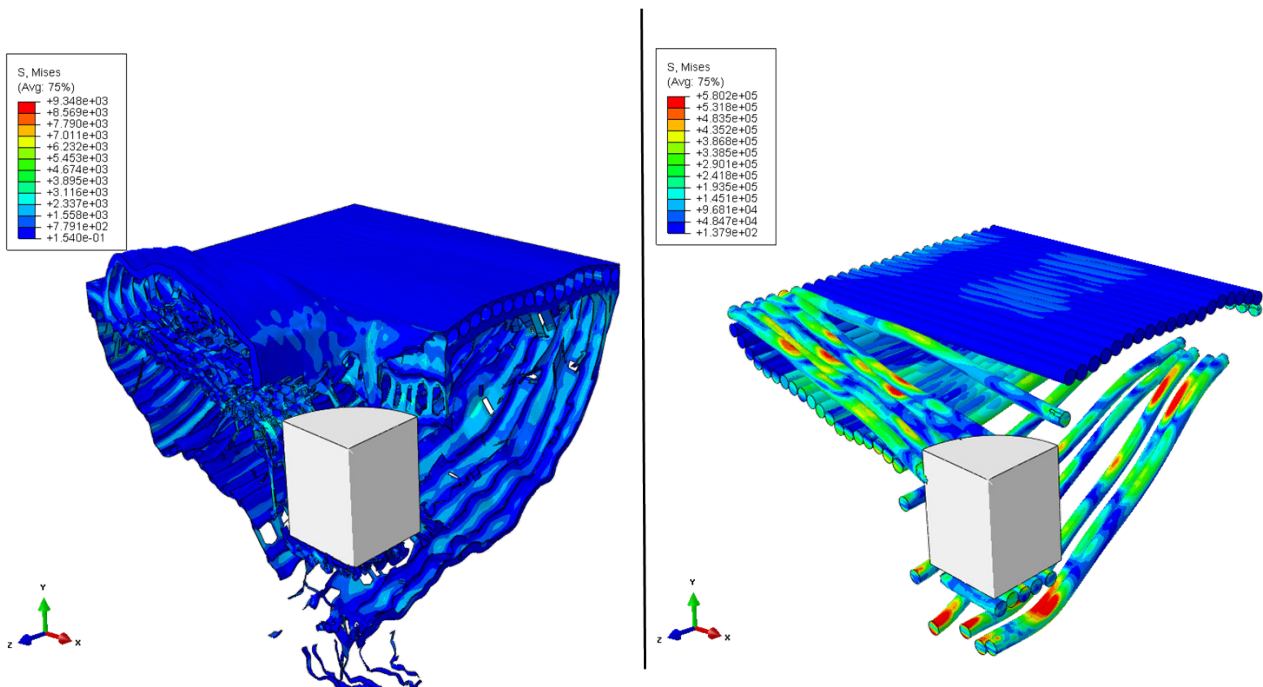


Figure 10. Von Mises Stress Contours in the Kraton-D Matrix (left) and UHMWPE Fibers (right) for the Ballistic Loading Case (Shown at Time $t = 1.2 \mu s$)

Figure 11 depicts the energy dissipated by damage for the epoxy matrix (A – C) and the Kraton matrix (D – F) for the blast (top (A and D)), shock (middle (B and E)), and ballistic (bottom (C and F)) loading events. The inset plot in (A) shows the slight increase in the matrix shearing (blue line) curve. The four failure mechanisms are depicted as fiber breakage (green line), matrix shearing (blue line), and fiber/matrix cohesive failure (red line). Cohesive failure was a dominant energy dissipation mechanism for both the blast and shock cases. There was no energy dissipation from fiber breakage or matrix shearing in the shock case. Minimal energy dissipation through matrix shearing occurred in the blast case, and it was only evident near the end of the simulation (blue line).

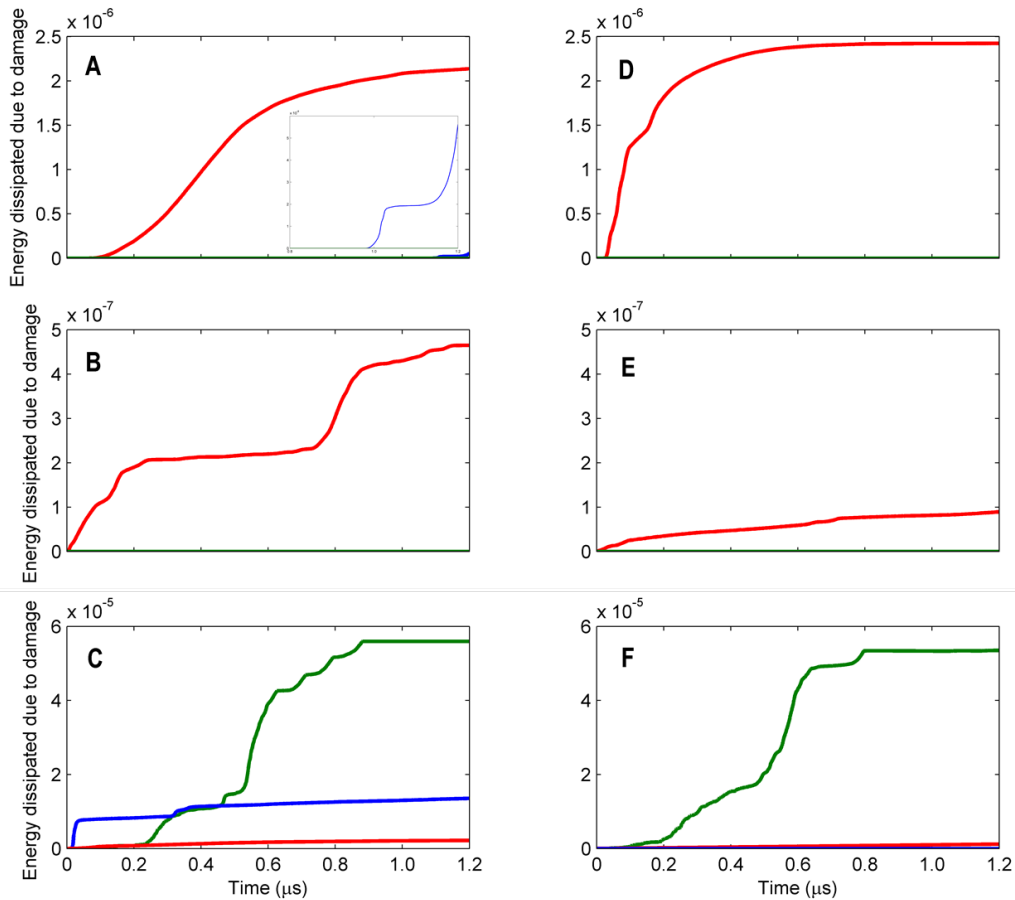


Figure 11. Energy Loss Due to Damage for the Epoxy Matrix (A – C) and the Kraton-D Matrix (D – F) for the Blast (top), Shock (middle), and Ballistic Impact (bottom) Loading Events

All failure modes contributed to the energy dissipation for the ballistic case, with fiber breakage being the most dominant. Matrix shearing played a larger role in dissipating energy in the epoxy matrix (C) than in the Kraton-D matrix (F) for the ballistic case because of the elastomeric behavior of the Kraton-D matrix, which must severely elongate before failure develops. The cohesive failure dissipates roughly the same amounts of energy. To illustrate this further, refer to figures 5 through 9, which illustrate the composite laminate following the dynamic loading event. Note that, in both the blast (figures 5 and 8) and shock (figures 6 and 9), very little fiber or matrix failure was observed—a finding also made apparent when the developed Von Mises stress was less than the ultimate strength of the matrix. For the ballistic case, in both the epoxy matrix (figure 7) and Kraton-D matrix (figure 10), the projectile plunged through the composite laminate. All the fiber and matrix elements failed in the area of the projectile. In addition, the fibers delaminated from the matrix along the boundary of the composite. These two factors are why the energy dissipation due to damage in the ballistic impact case was much higher than those produced in the blast and shock cases.

Figure 12 depicts the cohesive surfaces for the top ply (top row) and bottom ply (bottom row) for the fiber/matrix interfacial debonding and delamination for the epoxy matrix material for blast (column A), shock (column B), and ballistic impact (column C). Likewise, figure 13 depicts the cohesive surface damage results for the Kraton-D matrix material. In these figures, a value of 0 (blue) indicates that the threshold values for debonding have not been reached, and, therefore, cohesive failure had not yet initiated. A value of 1 (red) indicates that a fiber/matrix contact pair has completely delaminated.

In both matrix materials for the blast (column A) and ballistics (column C) case, the fiber and matrix have delaminated from each other at almost all interfacial points. There are slightly more cohesive failures in the blast and ballistic impact cases for the Kraton-D matrix (figure 13) than for the epoxy case (figure 12) because of the high elongation to failure afforded by the Kraton-D matrix. The cohesive failures for the shock case (column B, figures 12 and 13) were more uniform across the length of the composite with the Kraton-D matrix, but more failures were observed in the epoxy case for the top ply. Additionally, for the shock case, there were more cohesive failures in the bottom ply of the Kraton-D matrix (column B, bottom, figure 13) than the bottom ply of the epoxy matrix (bottom, figure 12).

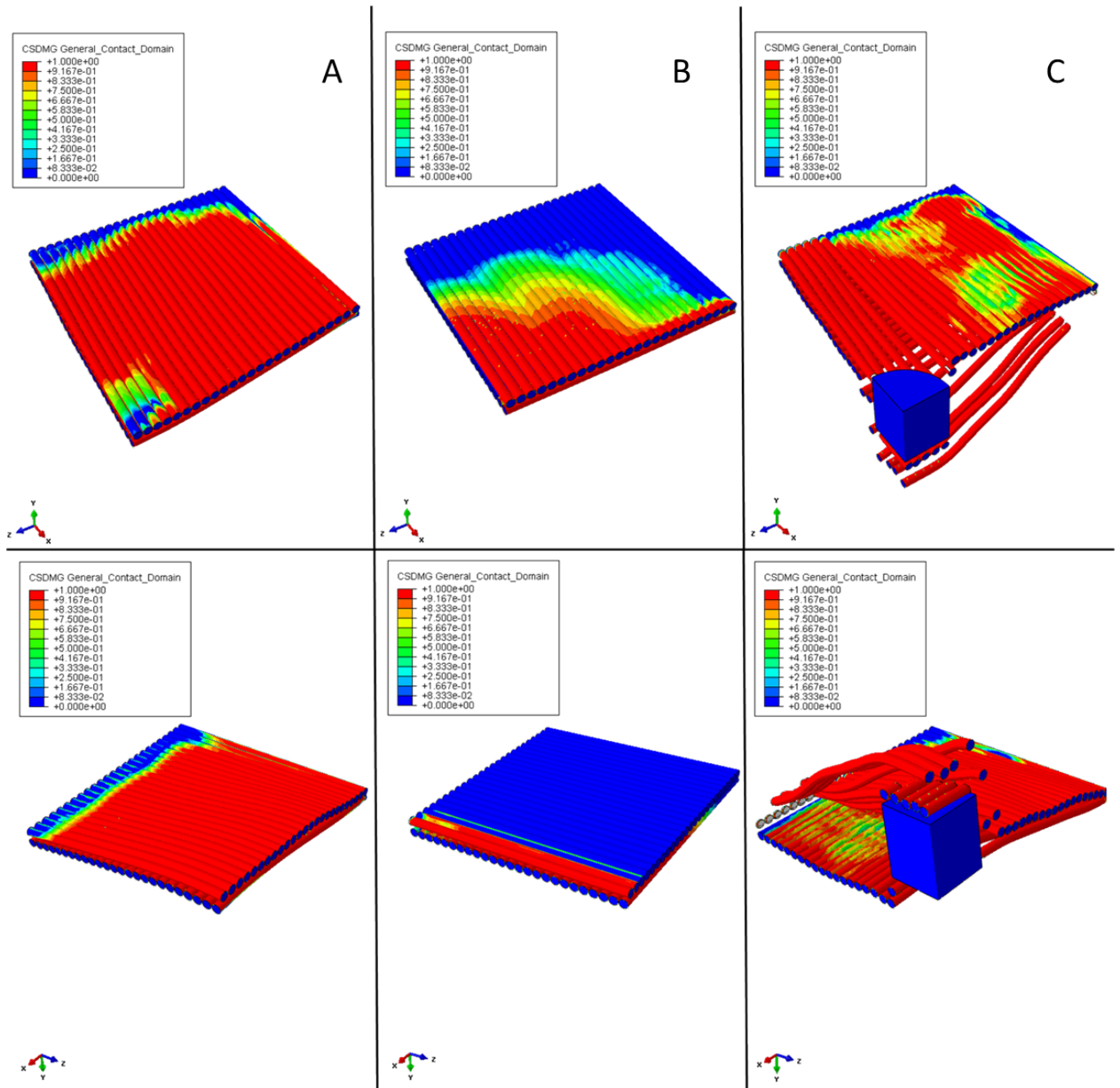


Figure 12. Depiction of the Cohesive Surfaces for the Top Ply (top row) and Bottom Ply (bottom row) for the Epoxy Material Subjected to Blast (column A), Shock (column B), and Ballistic Impact (column C)

(The scale ranges from 0-1 where a value of 1 means that the contact pair between that fiber and matrix have delaminated from each other. A value of 0 means that the contact pair has not yet experienced the onset of damage).

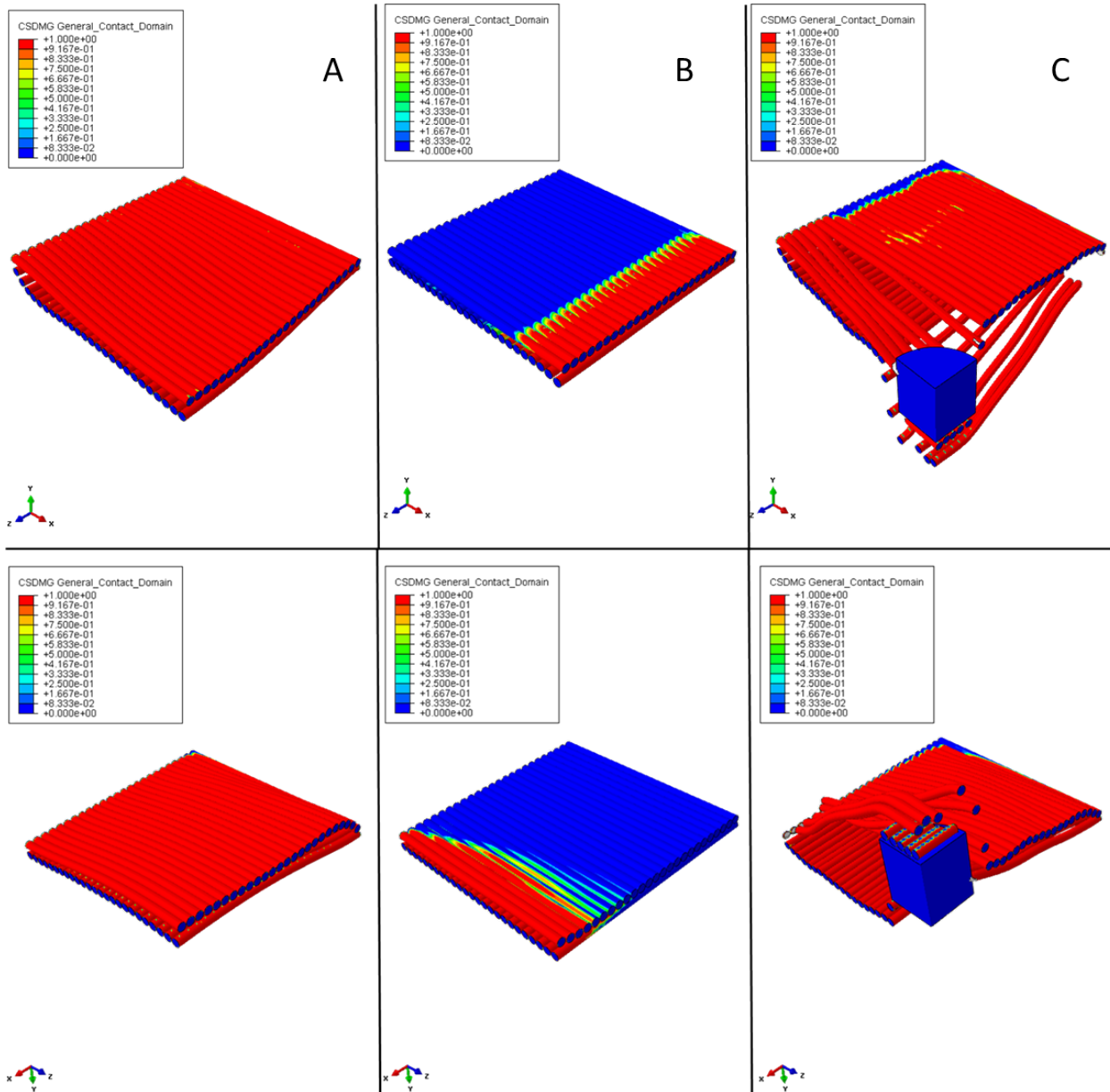


Figure 13. Depiction of the Cohesive Surfaces for the Top Ply (top row) and Bottom Ply (bottom row) for the Kraton-D Matrix Material Subjected to Blast (column A), Shock (column B), and Ballistic Impact (column C)

(The scale ranges from 0-1 where a value of 1 means that the contact pair between that fiber and matrix have delaminated from each other. A value of 0 means that the contact pair has not yet experienced the onset of damage).

Figure 14 depicts the velocity-time history of the projectile for the Kraton-D (blue line) and epoxy matrices (red line), respectively. The projectile in both models penetrated through the composite laminate at approximately 0.7 μs . The projectile's residual velocity was less for the epoxy matrix model versus the Kraton-D matrix model—suggesting that the epoxy matrix-reinforced laminate achieved a greater level of energy absorption.

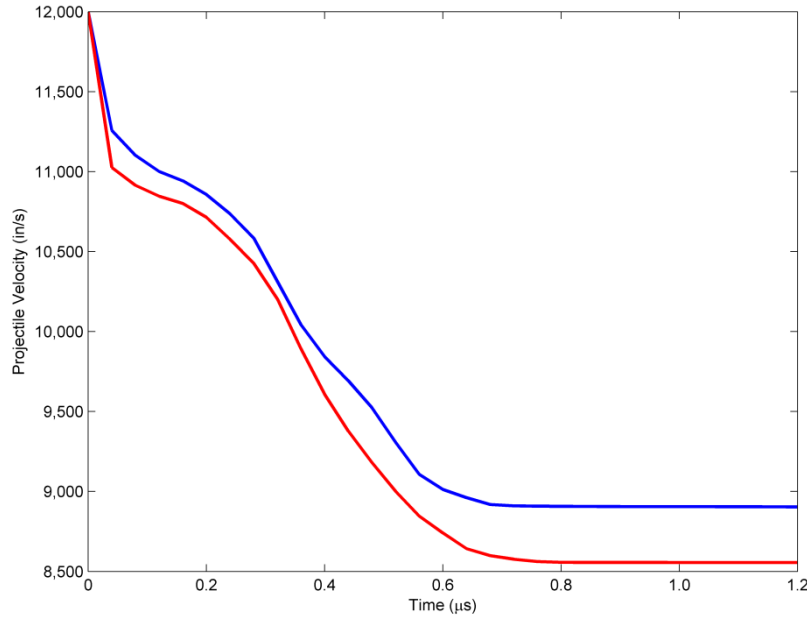


Figure 14. Projectile Velocity of the Kraton-D (blue line) and Epoxy (red line) Matrix

Figure 15 depicts the percentage of the total energy absorbed by the composite laminate from the projectile impact for the epoxy (red line) and Kraton-D (blue line) matrices. The total energy absorbed by the laminates consisted of the sum of the elastic strain energy, plastic strain energy, kinetic energy, damage dissipation energy, frictional dissipation energy, and viscous dissipation energy. In agreement with figure 14, the epoxy matrix composite absorbed slightly more energy than did the composite with the Kraton-D matrix. The two-ply epoxy matrix model absorbed 4.22% more of the energy in the same amount of time as did the two-ply model with the Kraton-D matrix for this particular ballistic impact event.

Time-history plots of each active energy absorption mechanism are presented in figure 16. Figure 16 (top) depicts the individual energy absorption terms for both the epoxy (column A) and Kraton-D (column B) matrix subjected to ballistic loading. The energy terms include damage dissipation (blue line), frictional dissipation (green line), kinetic energy of the composite (red line), elastic strain energy (magenta line), plastic strain energy (cyan line), and viscous dissipation (yellow line). The frictional energy was based on the use of static friction coefficients defined for contact between the projectile, fibers, and matrices. The viscous dissipation utilized a default value that ABAQUS included.

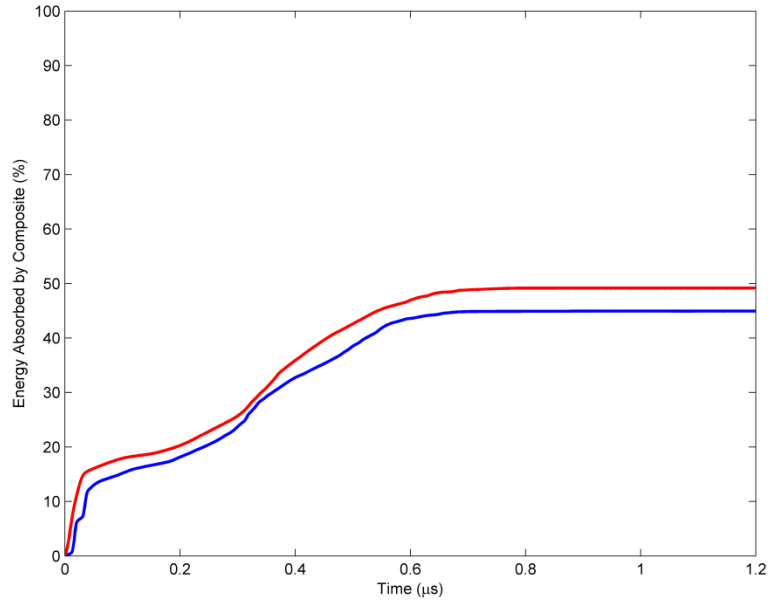


Figure 15. Percentage of the Projectile Kinetic Energy Absorbed by the Epoxy (red line) and Kraton-D (blue line) Composite Laminate

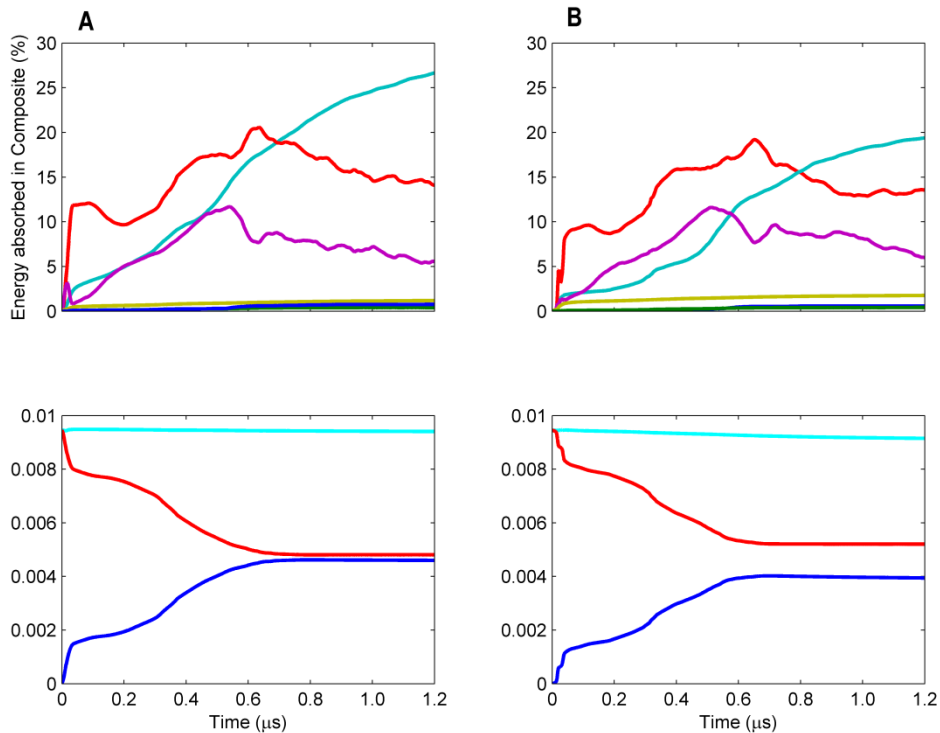


Figure 16. Top Row: Percentage of the Energy Absorption Mechanisms of the Composite Laminate Including Damage Dissipation (blue line), Frictional Dissipation (green line), Kinetic Energy of the Composite (red line), Plastic Dissipation (cyan line), Strain Energy (magenta line), and Viscous Dissipation (yellow line) for the Epoxy (column A) and Kraton-D (column B) Matrix Materials Subjected to Ballistic Loading; Bottom Row: Energy Balance (cyan line) Showing the Sum of the Energy Absorbed by the Composite (blue line) and the Kinetic Energy of Projectile (red line)

The sum of all energy terms is represented by the blue line in figure 16 (bottom); the kinetic energy of the projectile (red line), a replicate of figure 15, was added here for convenience. The sum of these two plots yields a constant value (cyan line) over the course of the simulation. Because this energy curve is constant, the time rate of change would yield a value of zero, indicating conservation of energy. Effectively, the figure is graphically showing that equation (9) is being satisfied, where the blue line is the right side of the equation and the difference of the cyan line and red line is the left side of the equation.

$$\frac{1}{2} m_{proj} (v_0^2 - v_f^2) = E_{plastic} + E_{elastic} + E_{frictional} + E_{damage} + E_{viscous} + E_{kinetic} \quad (9)$$

In both matrix composite configurations, the dictating energy absorption terms are the kinetic energy, elastic strain energy, and plastic strain energy of the composite.

DISCUSSION

The purpose of this research was to investigate the energy absorption capabilities of admissible failure modes for a cross-ply UD composite laminate subjected to severe dynamic loading events including blast, shock, and ballistic impact. The composite laminates used in this research were composed of hard (epoxy) and soft (Kraton-D) matrix materials. The fibers used in both matrix models were UHMWPE fibers. The simulation time of each loading case was 1.2 μ s.

Damage in the fibers, matrix, and cohesive interfaces was observed to be interdependent as the load path from the fiber to fiber-matrix interface to matrix was sequential. If the fiber and or matrix have failed at a particular region, then cohesive damage cannot initiate and accumulate at that region. The same is not true, however, for the reverse case. If a cohesive interface has delaminated, the fiber and the matrix at that region can still support stress and possibly lead to failure; therefore, all the cohesive interfaces can fail while the fiber and matrix continue to function and later experience damage initiation and evolution. This possibility is illustrated in the epoxy matrix case for the blast loading event (refer to figure 11 (A) and figure 12 (column A)). At the end of the simulation, almost all the cohesive surfaces have failed, which is indicated by a value of 1 (red). In addition, the dissipation due to cohesive damage plateaued in figure 11 (A (red line)); however, at approximately 1 μ s, with nearly all cohesive regions failed, matrix failure just initiated—depicted by the small curve representing matrix shearing in figure 11 (A (blue line)). Further blast loading increased matrix failures despite a majority of the cohesive contact regions delaminating.

Compared to fiber breakage and matrix shearing, cohesive damage was the dominant damage mechanism for energy dissipation in both the blast and shock cases for both the epoxy and Kraton-D matrix material models. The amounts of energy dissipation through cohesive damage in the epoxy and Kraton-D matrix models were roughly the same for the respective blast cases; however, the Kraton-D matrix models achieved this amount at a much faster rate than did

the epoxy matrix models. The faster rate was attributed to the lower cohesive strength of the Kraton-D matrix in contrast to that of epoxy. Fiber-to-matrix delamination develops faster in time for matrices having lower cohesive strengths in a given blast event. This important observation is critical to the design of protective composites for blast loading in which fiber-to-matrix cohesive damage is a necessary mechanism for energy dissipation.

Results of the shock loading case revealed that the accumulation of cohesive damage occurred earlier in time and to a greater extent for the epoxy matrix model than for the Kraton-D matrix model. Here, the fibers were loaded along their longitudinal axis compressing the matrix material. A matrix material that is weaker than the fiber tries to peel itself back down the length of the fiber. Because the epoxy matrix material is more compressible than is the elastomeric Kraton-D material, it will experience more cohesive failure than will Kraton-D material.

The dominant damage mechanism for the ballistic impact case was fiber breakage (followed by appreciable matrix shearing for the epoxy matrix model). As the projectile sheared through the material (referred to as “plug formations”), the primary fibers and matrix elements at the projectile contact region failed by shearing through the laminate. Furthermore, additional failures of the primary fibers on the strike face and several secondary fibers on the rear face were observed along the model boundaries, thus increasing the total damage developed through fiber breakage. As in the blast and shock cases, the energy dissipation due to matrix shearing damage was notable in the epoxy matrix model and nearly negligible for the Kraton-D matrix model. The Kraton-D matrix did not appreciably resist shearing deformations because of its relatively high compliance and low shear strength. With the epoxy matrix, however, energy dissipation through matrix shearing damage was relatively low. Likewise, the cohesive damage energies for the Kraton-D and epoxy materials were also nearly negligible.

Figures 12 and 13 show that, for the ballistic impact case, both matrix materials experienced cohesive damage initiation nearly throughout the volumes of their respective models. Furthermore, nearly all the cohesive interface regions experienced damage initiation, which, for the Kraton-D matrix, led to full cohesive failures. The amount of cohesive damage energies, however, was nearly negligible—not surprising in that there were far fewer cohesive interface regions to fail compared to the number of fiber and matrix elements that could fail for a given fiber volume ratio V_f . Each fiber element, matrix element, and cohesive region that fails dissipates energy through damage. It is surmised, therefore, that laminated composites constructed of increasing values of V_f have a greater propensity than do laminated composites constructed of decreasing values of V_f to develop greater cohesive damage energies.

The epoxy matrix (red line in figure 14) absorbed more ballistic impact energy than did the Kraton-D matrix (blue line in figure 14) as evidenced by the projectile’s smaller residual velocity V_r , which is 2.9% less. Further evidence that the epoxy matrix absorbed more ballistic impact energy than did the Kraton-D matrix is shown in figure 15, which depicts the total kinetic energy of the projectile absorbed by the composite laminate. The energy absorbed using the epoxy matrix (red line) is 4.22% greater than that absorbed due to damage by the Kraton-D matrix (blue line).

The upper time history plots of figure 16 depict each of the energy terms of the ballistic impact case for the epoxy matrix (column A) and the Kraton-D matrix (column B). The dominating energy absorption mechanisms of the composite were the plastic strain energy, elastic strain energy, and kinetic energy. The remaining energy terms, roughly one order of magnitude less, were the viscous energy, damage energy, and frictional energy. Because energy was conserved, the total sum of the absorbed energies (blue line) and the kinetic energy of the projectile (red line) were plotted by a constant value curve (cyan line) in figure 16 (bottom). This constant value was the projectile's initial kinetic energy, thus confirming energy conservation.

Lastly, the epoxy matrix absorbed 49.17% of the initial projectile kinetic energy (4.22% more energy than that absorbed by the Kraton-D matrix); however, more matrix material was observed to have failed for the epoxy matrix than for the Kraton-D matrix. This finding suggests that full projectile arrest could be achieved by doubling the number of plies, resulting in an approximate V_0 -ballistic limit and the choice of matrix material will also dictate the amount of energy absorbed which becomes pivotal in composite design and optimization. Additionally, by accounting for all energy absorption and failure mechanisms, a manufacturer could better produce composite laminates by tailoring the matrix and fiber materials; tensile, shearing, and cohesive failure thresholds; and ply counts and stacking schedules to optimally defeat specific projectile threats.

CONCLUSIONS

This research centered on investigating the energy absorption capabilities of failure modes in unidirectional laminated composites subjected to various dynamic loading conditions including blast, shock, and ballistic impact. Four failure mechanisms were considered: fiber breakage, matrix shearing, fiber delamination, and matrix delamination (that is, cohesive failure). Two matrix materials, a rigid epoxy and a compliant elastomer (Kraton-D), were evaluated. The reinforcing fiber material was ultrahigh molecular weight polyethylene.

The results suggest that the energy dissipated through cohesive failure mechanisms must be accounted for in the blast and shock events. The rate at which energy was dissipated through cohesive damage for the blast case differed for the two matrix materials; however, the amount of energy dissipated through cohesive failures was nearly invariant for the two matrices. For the shock event, the epoxy matrix dissipated more energy through cohesive damage than did the Kraton-D matrix. All damage mechanisms must be accounted for in ballistic impact events; however, fiber breakage was the most dominant damage energy mechanism. It was shown that the epoxy matrix better minimized the projectile's residual velocity and absorbed 4.22% more dynamic energy. More matrix material, however, has failed.

While the threshold values of damage initiation and evolution used throughout this study were limited to single values, the inclusion of cohesive failure modes was shown to be critical in developing robust FE models for both blast and shock events. Material properties including

failure thresholds must be obtained through experiments conducted on the fibers, matrix, and the composite laminate system.

The authors acknowledge that this research considered only one fiber volume ratio V_f and that future studies should address the effects of matrix-rich and matrix-starved constructions. Similarly, the ballistic impact case assumed a rigid (nondeforming) projectile with a right circular cylinder shape. Other projectile types and velocities should be included in future studies.

REFERENCES

1. P. V. Cavallaro, "Soft Body Armor: An Overview of Materials, Manufacturing, Testing, and Ballistic Impact Dynamics," NUWC-NPT Technical Report 12,057, Naval Undersea Warfare Center Division Newport, RI 02841, 1 August 2011.
2. P. V. Cavallaro and A. M. Sadegh, "Crimp-Imbalanced Protective (CRIMP) Fabrics," NUWC-NPT Technical Report 11,957, Naval Undersea Warfare Center Division Newport, RI 02841, 31 March 2010.
3. A. M. Sadegh and P. V. Cavallaro, "Crimp-Imbalanced Protective (CRIMP) Fabrics: An Analytical Investigation into the Relationship Between CRIMP Contents, Energy Absorption, and Fabric Ballistic Performance," NUWC-NPT Technical Report 11,970, Naval Undersea Warfare Center Division Newport, RI 02841, 15 September 2010.
4. L. Mishnaevsky and P. Brondsted, "Micromechanical Modeling of Damage and Fracture of Unidirectional Fiber Reinforced Composites: A Review," *Computational Materials Science*, vol. 44, pp. 1351 – 1359, 2009.
5. A. Tabiei and G. Nilakantan, "Ballistic Impact of Dry Woven Fabric Composites: A Review," *Applied Mechanics Reviews*, vol. 61, 2008.
6. R. M. Jones, *Mechanics of Composite Materials*, Taylor & Francis Group, LLC, New York, NY, 1999.
7. N. M. Hassan and R. C. Batra, "Modeling Damage in Polymeric Composites," *Composites: Part B*, vol. 39, pp. 66 – 82, 2008.
8. R. C. Batra and N. M. Hassan, "Blast Resistance of Unidirectional Fiber Reinforced Composites," *Composites: Part B*, vol. 39, pp. 513 – 536, 2008.
9. R. C. Batra and N. M. Hassan, "Response of Fiber Reinforced Composites to Underwater Explosive Loads," *Composites: Part B*, vol. 38, pp. 448 – 468, 2007.

10. F. Dolce, M. Meao, A. Wright, and M. French, "Structural Response of Laminated Composite Plates to Blast Load," *Plastics, Rubber, and Composites*, vol. 39, pp. 180-188, 2010.
11. M. A. Will, T. Franz, and G. N. Nurick, "The Effect of Laminate Stacking Sequence of CFRP Filament Wound Tubes Subjected to Projectile Impact," *Composite Structures*, vol. 58, pp. 259 – 270, 2002.
12. C. Balzani and W. Wagner, "An Interface Element for the Simulation of Delamination in Unidirectional Fiber-Reinforced Composite Laminates," *Engineering Fracture Mechanics*, vol. 75, pp. 2597 – 2615, 2008.
13. M. E. Walter, G. Ravichandran, and M. Ortiz, "Computational Modeling of Damage Evolution in Unidirectional Fiber Reinforced Ceramic Matrix Composites," *Computational Mechanics*, vol. 20, pp. 192 – 198, 1997.
14. S. Maiti and P. H. Geubelle, "A Cohesive Model for Fatigue Failure of Polymers," *Engineering Fracture Mechanics*, vol. 72, pp. 691 – 708, 2005.
15. M. Karahan, "Comparison of Ballistic Performance and Energy Absorption Capabilities of Woven and Unidirectional Aramid Fabrics," *Textile Research Journal*, vol. 78, pp. 718 – 730, 2008.
16. G. C. Jacob, J. F. Fellers, S. Simunovic, and J. M. Starbuck, "Energy Absorption in Polymer Composites for Automotive Crashworthiness," *Journal of Composite Materials*, vol. 36, pp. 813 – 850, 2002.
17. ABAQUS/Explicit, Version 6.11, ABAQUS. Inc, Pawtucket, RI, 2011.
18. M. Grujicic, G. Arakere, T. He, W. C. Bell, B. A. Cheeseman, C. F. Yen, and B. Scott, "A Ballistic Material Model for Cross-Plied Unidirectional Ultra-High Molecular-Weight Polyethylene Fiber-Reinforced Armor-Grade Composites," *Materials Science and Engineering A*, vol. 498, pp. 231 – 241, 2008.

INITIAL DISTRIBUTION LIST

Addressee	No. of Copies
Office of Naval Research (ONR-311 (Reza Malek-Madani), ONR-331 (R Barsoum))	2
U.S. Army Research Laboratory Weapons and Materials Research Directorate (AMSRD-ARL-WM-MD (B. Cheeseman))	1
Defense Technical Information Center	2
Center for Naval Analyses	1

